UC Santa Barbara

UC Santa Barbara Previously Published Works

Title

Radial Anisotropy in Receiver Function H-κ Stacks

Permalink

https://escholarship.org/uc/item/1v84349s

Authors

Brunsvik, Brennan
Eilon, Zachary

Publication Date

2023-10-26

DOI

10.1785/0220230114

Peer reviewed

Radial Anisotropy in Receiver Function H-κ Stacks

Brennan Brunsvik[*1] and Zachary Eilon[1]

Abstract

Receiver functions can be used to estimate the Moho depth (*H*) and ratio of *P* to *S* wavespeed (α/β or κ) in the crust. This is commonly done by grid search, forward modeling travel times to produce so-called "*H*-κ" stacks of receiver function amplitude. However, radial anisotropy in the crust, which can be significant, is almost never considered in this process. Here, we show that radial anisotropy changes the *H*-κ stack, biasing interpretations of crustal structure by introducing errors up to ∼3% in *H* and ∼1% in κ for commonly observed anisotropy magnitudes. We propose a simple method to correct *H*-κ stacks by incorporating radial anisotropy in the forward calculation. Synthetic tests show that this approach almost completely removes error caused by radial anisotropy. We show examples of this procedure with stations in the eastern United States. We provide readers with code to construct radially anisotropic *H*-κ stacks.

Introduction

Receiver functions are frequently used to measure the depths to seismic discontinuities in the Earth. *P*-to-*s* receiver functions utilize the timing of *P*-wave conversions and reverberations from velocity boundaries to identify the depths of those boundaries (e.g., Langston, 1979). *H*-κ stacking is a particular waveform stacking method that provides depth to the Moho (e.g., Zhu and Kanamori, 2000).

Receiver functions and *H*-κ stacking are powerful tools. They can be constructed with just one seismometer, making them broadly useful across the world, in remote regions, and even in planetary seismology (e.g., Kim *et al.*, 2021; Lognonné *et al.*, 2003). They have been used to construct large-scale maps of the Moho over, for example, the whole United States (Crotwell, 2007) and China (Li *et al.*, 2014). *H*-κ stacks can also provide complementary constraints to other data, for example surface waves, to vastly improve Earth models (e.g., Petruska and Eilon, 2021).

When a *P* wave encounters a velocity discontinuity, energy from this "parent" pulse is transmitted and converted as *p* and *s* "daughter" pulses, which may in turn reflect and reverberate. A receiver function is a Green's function that, when convolved with the parent pulse, reproduces the daughter wavetrain. A standard approach to construct *Ps* receiver functions is to take the parent *P* waveform on the *P* component, and deconvolve this from the *SV* component (e.g., Langston, 1979).

The timing of each phase in a receiver function is primarily controlled by the Moho depth (*H*) and the average α/β ratio in t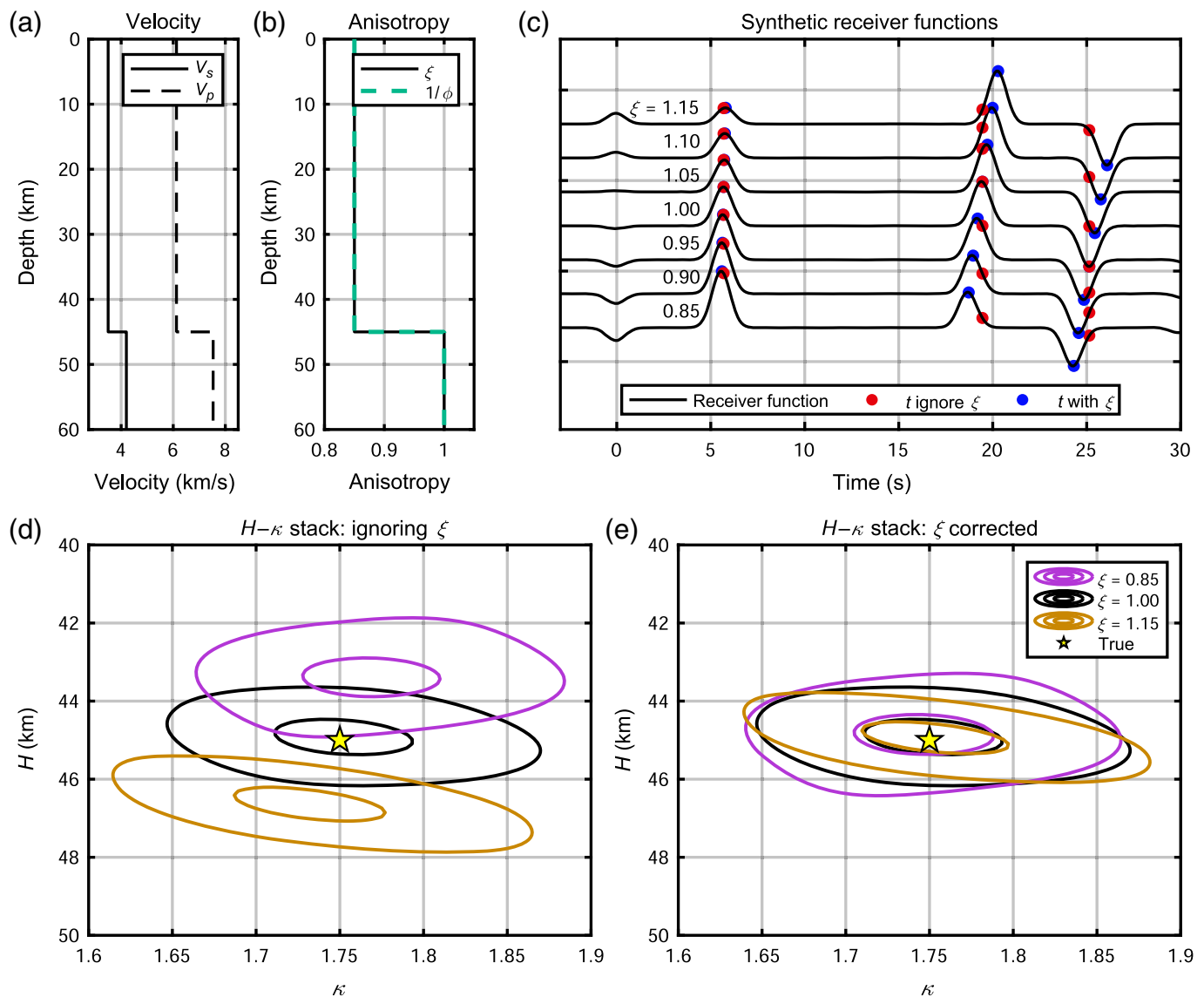he crust (κ). Researchers can stack waveform amplitudes at times predicted for *Ps*, *PpSs*, *PsPs*, and *PpPs* pulses based on assumed *H* and κ values to provide a map that is directly interpretable in terms of *H* and κ (Zhu and Kanamori, 2000; Fig. 1d). A grid search over *H* and κ (an *H*-κ stack) should have the highest amplitude at the true *H* and κ.

The *H*-κ stack method traditionally assumes that the crust is isotropic. However, seismic anisotropy, the variation in seismic wavespeed with direction or polarity of wave propagation, can be strong. This article is focused on radial anisotropy, the variation in wavespeed for vertically (e.g., V_{SV}) versus horizontally polarized waves (e.g., V_{SH}). Azimuthal anisotropy instead refers to wavespeed variation with azimuth (Maupin and Park, 2007), which we do not address in the method presented here. Individual crustal minerals can have *S*-wave anisotropy of 55% in plagioclase, 71% in alkali feldspars, 40% in quartz, and 100% in micas (Babuška, 1982). Natural crustal rock samples from the Basin and Range (U.S.A.) reach $\xi = V_{SH}^2/V_{SV}^2 = 1.23$ (Erdman *et al.*, 2013). Shape preferred orientation, for example, from aligned melt or layers of rock with contrasting properties also causes anisotropy (e.g., Jiang *et al.*, 2023). Examples of strong radial anisotropy in the crust derived from Rayleigh and Love waves include up to $\xi \approx 0.85$ to $\xi \approx$

1. Department of Earth Science, University of California, Santa Barbara, California, U.S.A., https://orcid.org/0000-0002-8559-026X (BB); https://orcid.org/0000-0002-4373-646X (ZE)

*Corresponding author: brennanbrunsvik@ucsb.edu

Figure 1. Synthetic receiver functions in the presence of radial anisotropy and H-κ stacks accounting for and ignoring the anisotropic terms. (a) Example of velocity model used in synthetic tests with $H = 45$ km. (b) Example of anisotropy model used in synthetic test with $\xi = 0.85$. (c) Resulting synthetic receiver functions with ξ varying from 0.85 to 1.15. Using the known H, κ, and average crustal V_p, we estimated the timing of receiver function pulses. We calculated pulse times while ignoring anisotropy ($\xi = 1$), shown as red dots, and including anisotropy, shown as blue dots. (d) H-κ stack for three values of ξ (panel e, see inset), in which anisotropy corrections were not applied. Contours are plotted at 95% and 70% of the maximum value in each H-κ stack. (e) Same as panel (d), but with anisotropy corrections applied. The color version of this figure is available only in the electronic edition.

1.15 in southern Madagascar (Dreiling *et al.*, 2018) and $\xi \approx 0.80$ to $\xi \approx 1.2$ in the Central Andes (Lynner *et al.*, 2018).

Radial anisotropy causes error in H-κ stacks (Hammond, 2014). However, a correction for radial anisotropy has not previously been developed. Previous workers have adapted the H-κ stacking method to account for azimuthal anisotropy (Hammond, 2014; Kaviani and Rümpker, 2015; Li *et al.*, 2019; Wen *et al.*, 2019). These methods tended to rely on shear-wave splitting and back-azimuthal variations in receiver functions, neither of which is clearly produced by radial anisotropy, necessitating development of a different method.

In this article, we evaluate the influence of radial anisotropy on H-κ stacks. We propose a simple method to correct H-κ stacks for radial anisotropy, in which we account for anisotropic velocities for each ray traversing the crust. We use synthetic tests to quantify the error introduced by ignoring anisotropy when making H-κ stacks and show that the error is removed after

applying our anisotropy correction. We apply the anisotropy correction to stations in the eastern United States. We include code for other researchers to apply the correction.

Method

Anisotropic *H*-*κ* stack

To construct *H*-*κ* stacks from receiver functions, we follow a similar procedure to Zhu and Kanamori (2000). However, we substitute isotropic velocities with anisotropic velocities (V_P and V_{SV}; assuming energy remains polarized in the vertical–radial plane) when estimating the timings of pulses. In this section, we describe how we construct and solve an elastic tensor to get these anisotropic velocities and pulse timings.

We assume a hexagonally symmetric elastic tensor with a vertical symmetry axis. This tensor can be expressed with the five Love parameters *A*, *C*, *F*, *L*, and *N*. The Love parameters can be calculated given α (*P* velocity), β (*S* velocity), ξ (*S* radial anisotropy), ϕ (*P* radial anisotropy), and η (which influences the ellipticity of the slowness surface). For clarity, we write α and β to indicate Voigt average *P* and *S* wavespeeds. We write V_{SV} and V_{SH} to indicate actual ray velocities of vertically and horizontally polarized shear waves, which depend on incidence angle. By assuming relationships between these elastic parameters, only ξ and V_P must be known to apply our anisotropic *H*-*κ* stacking. We assume that $V_{SH}/V_{SV} = V_{PH}/V_{PV}$, and thus $\phi = 1/\xi$. We assume $\eta = 1$ (e.g., Eilon *et al.*, 2016). *H*-*κ* stacking solves for $\beta = \alpha/\kappa$.

We use Voigt averaging to define the velocities of *P* and *S* waves traveling parallel and perpendicular to the symmetry axis (Panning and Romanowicz, 2006):

$$\alpha_\| = \alpha\sqrt{5\phi/(\phi+4)}, \quad \alpha_\perp = \alpha\sqrt{5/(\phi+4)},$$
$$\beta_\| = \beta\sqrt{3/(\xi+2)}, \quad \beta_\perp = \beta\sqrt{3\xi/(\xi+2)}. \tag{1}$$

We then calculate the Love parameters (Maupin and Park, 2007):

$$A = \rho\alpha_\perp^2,$$
$$C = \rho\alpha_\|^2,$$
$$L = \rho\beta_\|^2,$$
$$N = \rho\beta_\perp^2,$$
$$F = \eta(A - 2L). \tag{2}$$

Solutions to the Christoffel equations give three velocities for rays as a function of incidence angle, θ. We use the analytical expressions for ray velocities from Mavko *et al.* (2020):

$$V_P(\theta) = (A\sin^2\theta + C\cos^2\theta + L + \sqrt{M})^{1/2}(2\rho)^{-1/2},$$
$$V_{SV}(\theta) = (A\sin^2\theta + C\cos^2\theta + L - \sqrt{M})^{1/2}(2\rho)^{-1/2},$$
$$V_{SH}(\theta) = (N\sin^2\theta + L\cos^2\theta)^{1/2}(\rho)^{-1/2}, \tag{3}$$

in which

$$M = [(A-L)\sin^2\theta - (C-L)\cos^2\theta]^2 + (F+L)^2\sin^2 2\theta. \tag{4}$$

We substitute these anisotropic velocities into the standard equations of Zhu and Kanamori (2000) to calculate timings of *Ps*, *PpPs*, *PpSs*, and *PsPs* phases in receiver functions while accounting for radial anisotropy:

$$t_{P_s} = H\left(\sqrt{V_{SV}(\theta_s)^{-2} - p^2} - \sqrt{V_{PV}(\theta_p)^{-2} - p^2}\right),$$
$$t_{PpPs} = H\left(\sqrt{V_{SV}(\theta_s)^{-2} - p^2} + \sqrt{V_{PV}(\theta_p)^{-2} - p^2}\right),$$
$$t_{PpSs+PsPs} = 2H\sqrt{V_{SV}(\theta_s)^{-2} - p^2}, \tag{5}$$

in which *p* is ray parameter, and the incidence angles for *S* and *P* waves are $\theta_s = \sin^{-1}(\beta p)$ and $\theta_p = \sin^{-1}(\alpha p)$. This approach allows us to simultaneously include data from multiple events by correctly accounting for the moveout of all phases.

To form the stack, we grid search over *H* and *κ* and sum the amplitude of all receiver functions at the predicted times of each phase. We hold ξ and α constant. As we vary κ, $\beta = \alpha/\kappa$ also changes. Thus, equations (1)–(5) must be recalculated accordingly for each trial κ value.

Forward modeling and receiver function calculation

We used synthetic tests to evaluate the error in *H*-*κ* stacks with and without accounting for radial anisotropy. We calculated synthetic waveforms using the PropMat code (Keith and Crampin, 1977a,b,c). This allows a hexagonally symmetric elastic tensor with vertical symmetry. PropMat calculates transmission and reflection coefficients of rays through all layers in our model, and propagates a source function along all rays. We assumed a simple 2-s-wide Gaussian source function. For most synthetic tests, we used a ray parameter of $p = 6.15$ s/°, unless otherwise stated.

We test synthetic velocity models with two layers (crust and mantle) with constant properties with depth (Fig. 1a,b). A more complex model is shown in Figure S1, available in the supplemental material to this article. We calculated average crustal elastic parameters and density (ρ) after applying the Earth flattening transformation (e.g., Shearer, 2019).

We made receiver functions from the synthetic waveforms (Fig. 1c) as follows: we first rotated seismograms to the *P* and *SV* coordinate system (the incidence angle θ was inferred from the ray parameter). We applied the free-surface transform (Kennett, 1991). We used time-domain iterative deconvolution to deconvolve the source *P* waveform from the *SV* waveform (Ligorría and Ammon, 1999). We did not add noise because the goal is to examine offsets caused purely due to anisotropy (the influence of noise is instead shown in Fig. S2). From receiver functions, we make *H*-*κ* stacks based on equation (5). We used weights of 0.5, 0.3, and 0.2 for the *Ps*, *PpPs*, and *PpSs* + *PsPs* phases, respectively, in alignment with standard practices (e.g., Crotwell, 2007).
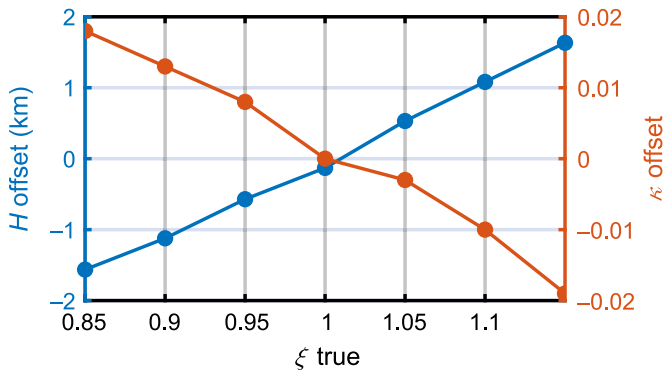
Figure 2. The difference between the true H and κ values and the solved H and κ values from maximizing the energy of H-κ stacks without accounting for anisotropy. We used true model values of $H = 45$ km and $\kappa = 1.75$. The color version of this figure is available only in the electronic edition.

"Phase weighting" is often used to improve the clarity of pulses in receiver functions before H-κ stacking (Schimmel and Paulssen, 1997; Crotwell, 2007). Phase weighting works under the assumption that the signal of interest is mostly the same on each time series, when the noise is not correlated. However, receiver function pulses vary in time based on the ray parameter. In practice, phase weighting still helps identify structures. However, we chose to avoid phase weighting for this study so that we could isolate only the effects of anisotropy on H-κ stacks.

Influence of Radial Anisotropy on H-κ Stacks
Synthetic H-κ stacks
Figure 1c shows the receiver functions and pulse timings predicted using $H = 45$ km and $\kappa = 1.75$, both including and ignoring anisotropy. When anisotropy is introduced, the estimated pulse timings are clearly misaligned with actual pulse timings. Although the misalignment is not visibly obvious for the Ps phase, mismatch is more prominent (up to about 1 s) for reverberated phases arriving after ~15 s. After applying the anisotropy correction, pulse times are accurately estimated.

For $\xi = 1$, the isotropically constructed H-κ stack correctly identified $H = 45$ km and $\kappa = 1.75$ (Fig. 1d). However, if there is substantial crustal anisotropy—in this case $\xi = 0.85$ or 1.15 —the assumption of isotropy leads to H being incorrectly estimated as 43.4 and 46.6, respectively, and κ as 1.768 and 1.731, respectively. In terms of fractional error, this equates to −3.5% and 3.6% in H, and 1.0% and −1.1% in κ. Although these errors are not large, they are also not randomly distributed—a region of substantial anisotropy will have systematically incorrect estimates of crustal parameters. After applying the anisotropy correction, the H-κ stack correctly identifies H and κ, regardless of ξ (Fig. 1e).

We applied the same synthetic test with a more complex model. We added a 0.5 km/s slow-velocity anomaly just beneath 10 km, and a 0.5 km/s fast-velocity anomaly just above 30 km (Fig. S1). The anisotropic stack is much closer to the true H and κ values. We also tested the influence of noise (Fig. S2). We added Gaussian noise before deconvolution, with a standard deviation of 4% of the amplitude of the parent pulse on the P component. The error in the anisotropic stack is greatly reduced compared with the isotropic stack. Only one receiver function was used in the H-κ stacks. With more receiver functions added, the results from the noisy H-κ stacks would asymptotically approach the H and κ values of the noise-free H-κ stacks shown in Figure 1.

Influence of Moho depth. We tested this anisotropy correction at a variety of Moho depths. For a given H, we tested values of $0.85 < \xi < 1.15$ and found the error in H and κ estimations. Figure 2 shows an example for $H = 45$ km. Figure 2 shows that the H and κ offset caused by ξ varies approximately linearly as a function of ξ, at least between $0.85 < \xi < 1.15$.

We tested $25 < H < 55$ km and find that the fractional error in H is not dependent on H: it is approximately

$$\Delta H/H \approx 0.25(\xi - 1). \tag{6}$$

So, for $\xi = 1.10$, the error in H will be roughly 2.5%. In other words, a region with double the Moho depth will have twice the absolute error in H estimations if one neglects to account for anisotropy.

Influence of ray parameter. The amount of anisotropy correction needed is dependent on the incidence angle of a ray (equation 5). We explore whether certain incidence angles and ray parameters will be more sensitive to anisotropy corrections when making H-κ stacks (Fig. 3).

We assumed $H_{\text{true}} = 45$ km and $\xi_{\text{true}} = 1.15$ to calculate a given phase timing t_{true} using equation (5). Then, using t_{true}, we solved equation (5) for H while assuming $\xi = 1$. This simulates the error in H that a researcher would encounter (for $\xi = 1.15$) if ξ were not accounted for. The percent error is not dependent on H_{true} (equation 6). H error generally increases with p (Fig. 3). Because different phases have different sensitivities to ξ, we show the percent error for each phase individually, as well as the average error from all phases. Average H error varies between about −1% and −7%, depending on both p and κ. The Ps phase gives H estimates that are most sensitive to ray parameter, from −8% down to 0%. $PpSs$ and $PsPs$ cap at about −5.5% error, and $PpPs$ caps at about −4.5% error. Figure 3 suggests that error could reach but should not exceed ~7% in H from ignoring ξ if $\xi = 1.15$.

Sensitivity of objective function to ξ. Incorrect assumption of isotropy when constructing the H-κ stack does
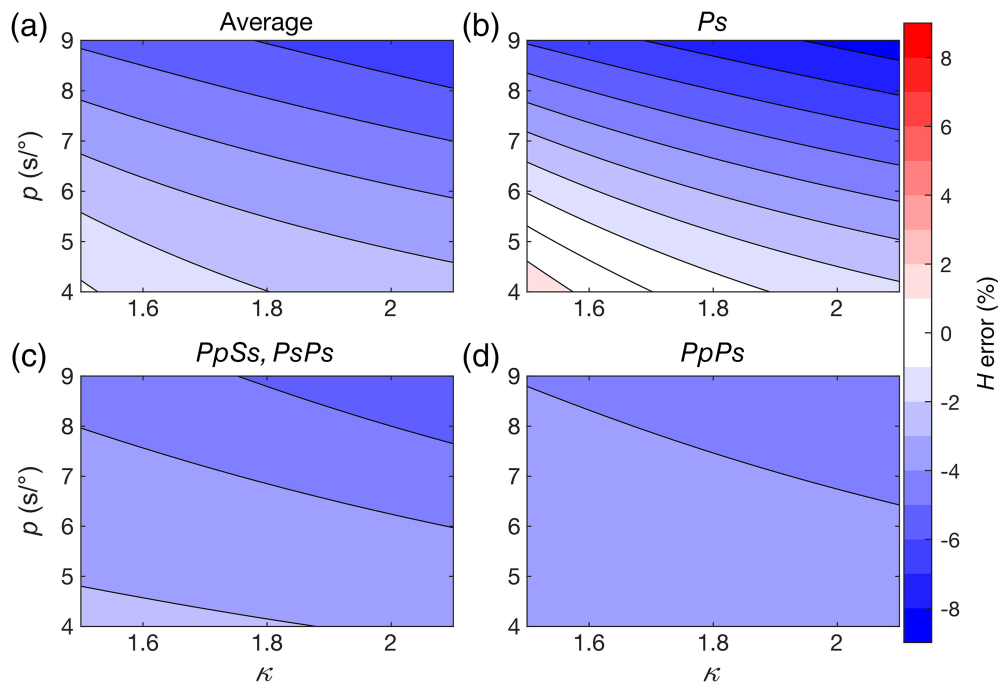
Figure 3. Shows the percent difference between true and predicted H as a function of ray parameter p and κ. We used $H = 45$ km and $\xi = 1.15$. The amount of error is different for different phases. (a) Error for each phase averaged. (b–d) Error for three isolated phases. The color version of this figure is available only in the electronic edition.

not simply lead to a shift in the stack maximum. It also reduces the amplitude of the maximum. This is because anisotropy introduces a ray-parameter-dependent shift in the crustal reverberation arrival times (Fig 1). Equation (5) cannot simultaneously predict the timing $t(H,\kappa)$ of all receiver function maxima if there is a substantial range in p. Thus, even the best-fitting time predictions miss the pulse maxima at the extreme values of p. However, by introducing an additional variable, equation (5) correctly identifies the pulse times $t(H,\kappa,\xi)$.

This article is focused on an approach to reduce bias caused in H-κ stacks from radial anisotropy. However, in theory, this approach can additionally be used to solve for radial anisotropy. Anisotropic H-κ stacking has previously been used to invert for anisotropy parameters (Hammond, 2014; Kaviani and Rümpker, 2015).

We tested the sensitivity of H-κ stacking to H, κ, and ξ. The derivative, or slope, of the energy in the H-κ stack as a function of H, κ, and ξ indicates the sensitivity to those parameters (Fig. 4). The sensitivity to H is greater than κ, which is greater than ξ. As an example, E (the amplitude of the H-κ stack) decreases to 90% of its maximum by perturbing H from 45.0 to 46.0 km, κ from 1.75 to 1.81, and ξ from 0.85 to 0.975. This H perturbation required is small, whereas this ξ perturbation is large. The H-κ stack is much more capable of identifying optimal H and κ than ξ.

This analysis demonstrates that receiver functions alone are unlikely to be sufficient to solve for ξ using this method. Instead, researchers should use ξ values that are obtained from other data, such as Love and Rayleigh waves, or take a joint inversion approach using receiver functions together with other data types.

Application to real data

We demonstrate the influence of anisotropy at a station with relatively high ξ (station KMSC from the Transportable Array; Fig. 5), and in the supplemental Text S1, station GOGA from the network US. At these stations, ξ is available from a recent inversion (Brunsvik et al., 2023) of Love and Rayleigh wave phase velocities (Ekström, 2017). Furthermore, these stations have relatively strong average crustal radial anisotropy at $\xi = 1.12$ for KMSC, and $\xi = 1.10$ for GOGA, which will illuminate the influence of anisotropy on H-κ stacks.

Station KMSC is in South Carolina, in the Piedmont between the Appalachian mountains and Atlantic. Station GOGA is in Georgia, near the transition from the Piedmont to the coastal plains. Various factors can contribute to anisotropy here, such as extension from the breakup of Pangaea, sills, or other remnant volcanic features (Withjack et al., 2012), mineral foliations and lineations that can be ubiquitous in the crust (Dalton and Gaherty, 2013), layered units, and complex faulting from thrusting and the assembly of Pangaea (Li et al., 2020), among other factors. A further geological interpretation is outside the scope of this article.

We used P-wave receiver functions from Incorporated Research Institutions for Seismology (IRIS)-EarthScope automated receiver survey (EARS; Crotwell, 2007; Fig. 5a). We added a quality control step, removing anomalous receiver functions defined by having low average autocorrelation to all other receiver function. We first remove receiver functions with < 0.85 correlation within −1 to 1 s of the parent pulse. We then repeat this culling procedure, now using minimum correlation of 0.40 up to 40 s after the parent pulse. For KMSC, this only removes one receiver function (out of 164), but this cross-correlation approach applies to other stations that can have more erroneous receiver functions.
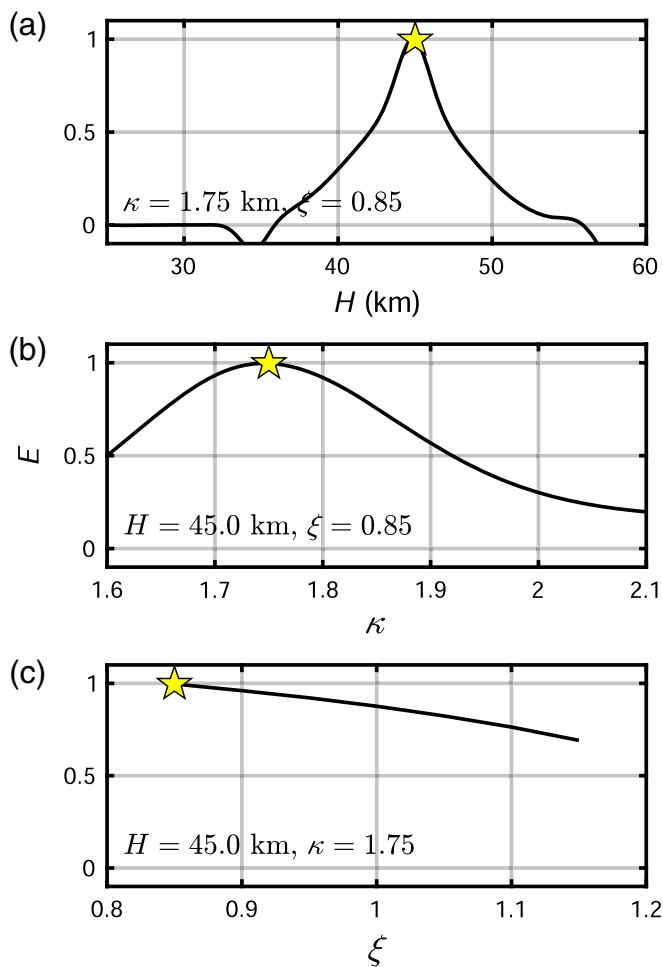
Figure 4. This shows the anisotropic H-κ stack amplitude as a function of (a) H, (b) κ, and (c) ξ. The yellow star indicates the true parameters used for this synthetic test. In each panel, the other two parameters are held fixed at their true values. The slope of E, the H-κ stack amplitude, can indicate the sensitivity of the H-κ stack to that parameter. The color version of this figure is available only in the electronic edition.

We constructed H-κ stacks for station KMSC, first ignoring and then accounting for radial anisotropy (Fig. 5b). The estimated H and κ are 31.73 km and 2.013 before incorporating radial anisotropy, and 30.92 km and 1.986 with radial anisotropy incorporated. H is shifted by -0.812 km (-2.558%), whereas κ is shifted by -0.027 (-1.347%). For station GOGA, the change in H was -1.082 km (-3.054%), whereas κ is shifted by -0.011 (-0.543%).

We used bootstrapping to test whether the changes in H and κ are statistically significant. For station KMSC, we resampled the receiver functions and applied H-κ stacking 200 times (Fig. S4). We obtained standard deviations of 0.18 for H and 0.012 for κ. These small standard deviations are partly owed to the large number of receiver functions used. This bootstrapping test suggests that the changes in H and κ are significant compared to the noise in the receiver functions, at 4.5 times the

standard deviation for H, and 2.6 times the standard deviation for κ.

The change in H from anisotropic H-κ stacking may also be significant compared with the input parameters. Zhu and Kanamori (2000) estimated that an uncertainty in V_p of 0.1 km/s leads to an uncertainty in H of $< \sim0.5$ km. The purpose of our tests on real data is demonstrative, and the error in V_p is highly dependent on the V_p model used, so we do not analyze the error in our chosen V_p model here.
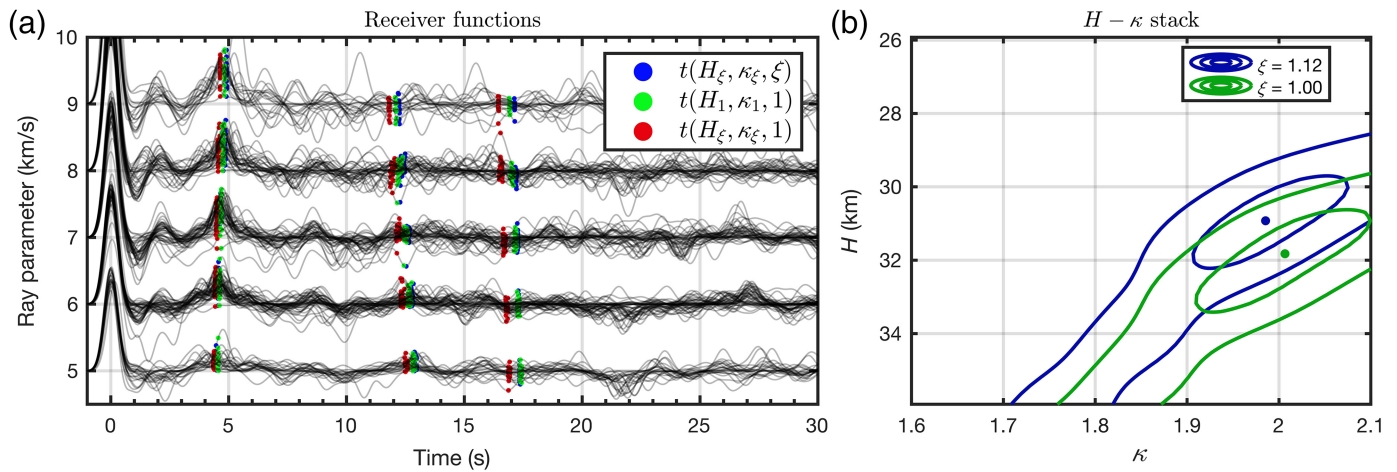
Changes in H from the anisotropic correction can be small but important. We demonstrate one possible consequence of changed H values with a simplified crustal extension and thinning exercise in the eastern United States. We assume the Piedmont and coastal plains had an initial crustal thickness of 40 km before breakup. We assume extension reached from the East Coast magnetic anomaly (Bécel *et al.*, 2020) to the Appalachian mountains, about 300 km. Thus, the isotropic $H = 31.73$ km implies 238.0 km original width, whereas the anisotropic $H = 30.92$ km implies 231.9 km original width, with a difference of 6.09 km original width. Small changes in H influence the stretching factor β. Assuming an initial crustal thickness of 40 km, the isotropic H solution leads to $\beta = 1.260$, whereas the anisotropic H solution leads to $\beta = 1.294$. Such considerations may be important in the Basin and Range, for example, to estimate extension and strain amounts.

To demonstrate the applicability of this radially anisotropic H-κ stacking method, we applied the procedure to stations in the eastern United States (Fig. 6). Average crustal ξ and V_p at each station are from Brunsvik *et al.* (2023). See supplemental text S1 for information. After applying the same cross-correlation criteria as with stations GOGA and KMSC, as well as other selection criteria that allow us to focus on stations with high-quality receiver functions (supplemental text S1), we kept 172 stations from US and TA networks. The resulting H values are similar to the results from Crotwell (2007) and Incorporated Research Institutions for Seismology Data Management Center (IRIS-DMC) (2010). H varies from ~30 km in the Coastal plains to ~40 km west of the Appalachians.

ξ is relatively large in the coastal plains and Piedmont of the eastern United States at about $\xi = 1.05$–1.1 (Fig. 6). At these locations, the change in H from applying the anisotropic versus isotropic H-κ stacking method was highest, at about -2%. The largest change in H was about 3% for $\xi \approx 1.1$. H, as well as the changes in H between the isotropic and anisotropic stacks, vary smoothly in space between most stations. The change in H as a function of ξ is linear and almost perfectly matches equation (6) (Fig. 6d). A least-squares fit of these results gives the change in H from anisotropic to isotropic H-κ stacking to be $\Delta H/H \approx 0.268(\xi - 1)$.

Discussion

The rotation to P and SV components and the free surface transform are affected by anisotropy. Figure 1 shows that

(a)

(b)

Figure 5. H-κ stacking on station KMSC from network TA, with and without anisotropy corrections. (a) Receiver functions from Incorporated Research Institutions for Seismology EarthScope automated receiver survey (IRIS-EARS) database (Crotwell, 2007; Incorporated Research Institutions for Seismology Data Management Center [IRIS-DMC], 2010). For each receiver function, we estimated the timing of each pulse using equation (5). The blue dots show timing predicted if we use H_ξ and κ_ξ, the parameters that give the highest amplitude in the anisotropy-corrected H-κ stack. The green dots shows timings that would be predicted through the standard H-κ stacking process: using the parameters H_1 and κ_1 that maximize the H-κ stack in which no anisotropy correction was performed. The red dots show timings predicted from equation (5) if H_ξ and κ_ξ are used, but when ξ is then set to 1. Note that this is not the same as what researchers would obtain under standard H-κ processing. Rather, the difference between the red and blue dots shows how much ξ alone shifts the pulse timings. Receiver functions are plotted by ray parameter, in which the ray parameter is rounded to the nearest integer. (b) H-κ stack made from receiver functions in panel (a), when anisotropy is accounted for (blue) or not accounted for (green). H_1 and κ_1 are picked from the green H-κ stack, and H_ξ and κ_ξ are picked from the blue H-κ stack. Contours for this plot are at 80% and 95% of the respective H-κ stack maxima. The color version of this figure is available only in the electronic edition.

the parent pulse at $t = 0$ s has nonzero amplitude in receiver functions when radial anisotropy is introduced. The parent pulse has no energy, as expected, if there is no anisotropy. One possible explanation is that shallow anisotropy changes the incidence angle of a ray. Standard methods for processing real receiver functions include a step to rotate seismograms in the direction that minimizes the parent pulse energy on the SV component. However, notable energy is almost always still present when applied to real receiver functions. Thus, radial anisotropy can cause this effect, along with other physical parameters.

Ignoring anisotropy when creating H-κ stacks can produce a systematically biased interpretation of H and κ. For $\xi > 1$, ignoring anisotropy causes estimates of H that are too deep (Figs. 1, 2, and 5). Continental crust tends to have radial anisotropy with $\xi > 1$ (Moschetti *et al.*, 2010; Dalton and Gaherty, 2013; Xie *et al.*, 2013), perhaps due to horizontal alignment of several intrinsically anisotropic minerals. For example, ~4%–5% peak–peak anisotropy ($\xi \sim 1.08$–1.1) is observed throughout western Canada and United States crust (Dalton and Gaherty, 2013; Xie *et al.*, 2015). This biases continental Moho estimates ~2% too deep in H-κ stacks according to equation (6). For example, the US average crustal thickness in the EARS database is 38.9 km (IRIS-DMC, 2010), which should shift slightly, but systematically to ~38.1 km if average $\xi = 1.08$, according to our synthetic tests (equation 6). Areas of active extension can have stronger anisotropy, in which it will be more important to incorporate radial anisotropy in H-κ stacks.

Conclusion

Radial anisotropy systematically influences H and κ estimated from receiver function stacks. Synthetic tests suggest that the fractional error in H estimates from ignoring ξ is $\Delta H/H \approx 0.25(\xi - 1)$. For strong anisotropy (e.g., $\xi = 1.15$), our synthetic tests showed ~3.6% error in H and -1.1% in κ. Our ξ correction eliminated this error in synthetic tests. Our example application in the Piedmont and coastal

plains in the eastern United States at station KMSC gave $H = 31.73$ km and $\kappa = 2.013$ with isotropic stacking. With anisotropic stacking and $\xi = 1.2$ (~5% anisotropy), we obtained $H = 30.92$ km and $\kappa = 1.986$. These changes could become important in dealing with, for example, crustal stretching. In any region with a reasonably well-known crustal ξ model, it is easy to adopt anisotropic H-κ stacking to minimize systematic biases in H and κ estimates. We release the code that we used to make anisotropic H-κ stacks.

Data and Resources

All receiver function waveform data are available through the Incorporated Research Institutions for Seismology Data Management Center (Crotwell, 2007; IRIS DMC, 2010; last accessed March 2023).
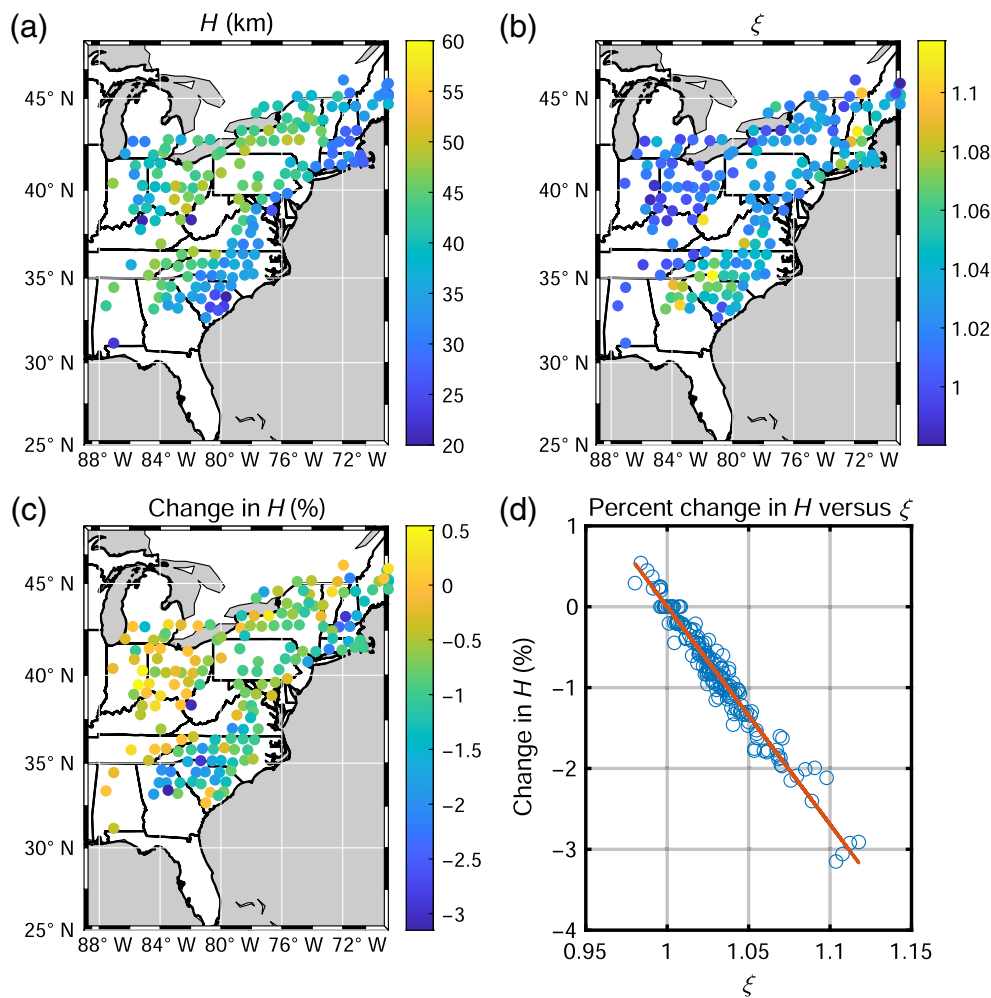
Figure 6. Anisotropic *H*-κ stacking applied to stations in eastern United States. (a) *H* (Moho depth) from anisotropic stacking. (b) ξ from Brunsvik *et al.* (2023). (c) Change in *H* between the anisotropic and isotropic *H*-κ stacks. (d) Change in *H* as a function of ξ, as well as a least-squares best-fit line. The color version of this figure is available only in the electronic edition.

We used network codes TA and US. Our anisotropic *H*-κ stack code is available at https://github.com/brennanbrunsvik/hk_anis (last accessed September 2023). V_s and ξ used for stations in eastern United States can be obtained from Brunsvik *et al.* (2023). The supplemental material contains more information about the ξ and V_s models used for applying *H*-κ stacking to real stations, synthetic receiver functions tests with noise and a more complex synthetic model, an example at US station GOGA, and a bootstrapping uncertainty analysis of TA station KMSC.

Declaration of Competing Interests

The authors acknowledge that there are no conflicts of interest recorded.

References

Babuška, V. (1982). Anisotropy of Vp and Vs in rock-forming minerals, *J, Geophys,* **50,** no. 1, 1–6.

Bécel, A., J. K. Davis, B. D. Shuck, H. J. A. Van Avendonk, and J. C. Gibson (2020). Evidence for a prolonged continental breakup resulting from slow extension rates at the eastern North American volcanic rifted margin, *J. Geophys. Res.* **125,** no. 9, 1–27.

Brunsvik, B., Z. Eilon, and C. Lynner (2023). *Lithospheric Structure and Mantle Flow at the Eastern North American Margin Identified from a Suite of Seismic Data Types,* SAGE/ GAGE Community Science Workshop, Pasadena, California, U.S.A.

Crotwell, H. P. (2007). *High Data Volume Seismology: Surviving the Avalanche,* Vol. 68, Citeseer, Columbia, South Carolina.

Dalton, C. A., and J. B. Gaherty (2013). Seismic anisotropy in the continental crust of northwestern Canada, *Geophys. J. Int.* **193,** no. 1, 338–348.

Dreiling, J., F. Tilmann, X. Yuan, J. Giese, E. J. Rindraharisaona, G. Rümpker, and M. E. Wysession (2018). Crustal radial anisotropy and linkage to geodynamic processes: A study based on seismic ambient noise in southern Madagascar, *J. Geophys. Res.* **123,** no. 6, 5130–5146.

Eilon, Z., G. A. Abers, and J. B. Gaherty (2016). A joint inversion for shear velocity and anisotropy: The Woodlark Rift, Papua New Guinea, *Geophys. J. Int.* **206,** no. 2, 807–824.

Ekström, G. (2017). Short-period surface-wave phase velocities across the conterminous United States, *Phys. Earth Planet. In.* **270,** 168–175.

Erdman, M. E., B. R. Hacker, G. Zandt, and G. Seward (2013). Seismic anisotropy of the crust: Electron-backscatter diffraction measurements from the Basin and Range, *Geophys. J. Int.* **195,** no. 2, 1211–1229.

Hammond, J. O. S. (2014). Constraining melt geometries beneath the Afar Depression, Ethiopia from teleseismic receiver functions: The anisotropic *H*-κ stacking technique, *Geochem. Geophys. Geosys.* **15,** no. 4, 1316–1332.

Incorporated Research Institutions for Seismology Data Management Center (IRIS DMC) (2010). Data services products: EARS EarthScope automated receiver survey, doi: 10.17611/DP/EARS.1.

Jiang, C., B. Schmandt, G. A. Abers, E. Kiser, and M. S. Miller (2023). Segmentation and radial anisotropy of the deep crustal magmatic system beneath the cascades arc, *Geochem. Geophys. Geosys.* **24,** no. 3, e2022GC010738, doi: 10.1029/2022GC010738.

Kaviani, A., and G. Rümpker (2015). Generalization of the H-κ stacking method to anisotropic media: Anisotropic H-κ stacking, *J. Geophys. Res.* **120,** no. 7, 5135–5153.

Keith, C. M., and S. Crampin (1977a). Seismic body waves in anisotropic media: Propagation through a layer, *Geophys. J. Int.* **49,** no. 1, 209–223.

Keith, C. M., and S. Crampin (1977b). Seismic body waves in anisotropic media: Reflection and refraction at a plane interface, *Geophys. J. Int.* **49,** no. 1, 181–208.

Keith, C. M., and S. Crampin (1977c). Seismic body waves in anisotropic media: Synthetic seismograms, *Geophys. J. Int.* **49,** no. 1, 225–243.

Kennett, B. L. N. (1991). The removal of free surface interactions from three-component seismograms, *Geophys. J. Int.* **104,** no. 1, 153–163.

Kim, D., V. Lekić, J. C. E. Irving, N. Schmerr, B. Knapmeyer-Endrun, R. Joshi, M. P. Panning, B. Tauzin, F. Karakostas, R. Maguire, *et al.* (2021). Improving constraints on planetary interiors with *PPs* receiver functions, *J. Geophys. Res. Planets* **126,** no. 11, doi: 10.1029/2021JE006983.

Langston, C. A. (1979). Structure under Mount Rainier, Washington, inferred from teleseismic body waves, *J. Geophys. Res.* **84,** no. B9, 4749.

Li, C., H. Gao, and M. L. Williams (2020). Seismic characteristics of the eastern North American crust with *Ps* converted waves: Terrane accretion and modification of continental crust, *J. Geophys. Res.* **125,** no. 5, 1–16.

Li, J., X. Song, P. Wang, and L. Zhu (2019). A generalized H-κ method with harmonic corrections on *Ps* and its crustal multiples in receiver functions, *J. Geophys. Res.* **124,** no. 4, 3782–3801.

Li, Y., M. Gao, and Q. Wu (2014). Crustal thickness map of the Chinese mainland from teleseismic receiver functions, *Tectonophysics* **611,** 51–60.

Ligorría, J. P., and C. J. Ammon (1999). Iterative deconvolution and receiver-function estimation, *Bull. Seismol. Soc. Am.* **89,** no. 5, 1395–1400.

Lognonné, P., J. Gagnepain-Beyneix, and H. Chenet (2003). A new seismic model of the Moon: Implications for structure, thermal evolution and formation of the Moon, *Earth Planet. Sci. Lett.* **211,** nos. 1/2, 27–44.

Lynner, C., S. L. Beck, G. Zandt, R. W. Porritt, F.-C. Lin, and Z. C. Eilon (2018). Midcrustal deformation in the central andes constrained by radial anisotropy, *J. Geophys. Res.* **123,** no. 6, 4798–4813.

Maupin, V., and J. Park (2007). Theory and observations—Wave propagation in anisotropic media, in *Treatise on Geophysics*, Elsevier, Vol. 1, 289–321.

Mavko, G., T. Mukerji, and J. Dvorkin (2020). *The Rock Physics Handbook*, Cambridge University Press, Cambridge, United Kingdom.

Moschetti, M. P., M. H. Ritzwoller, F. Lin, and Y. Yang (2010). Seismic evidence for widespread western-US deep-crustal deformation caused by extension, *Nature* **464,** no. 7290, 885–889.

Panning, M., and B. Romanowicz (2006). A three-dimensional radially anisotropic model of shear velocity in the whole mantle, *Geophys. J. Int.* **167,** no. 1, 361–379.

Petruska, J., and Z. Eilon (2021). Distributed extension across the ethiopian rift and plateau illuminated by joint inversion of surface waves and scattered body waves, *Geochem. Geophys. Geosys.* e2021GC010179, doi: 10.1029/2021GC010179.

Schimmel, M., and H. Paulssen (1997). Noise reduction and detection of weak, coherent signals through phase-weighted stacks, *Geophys. J. Int.* **130,** no. 2, 497–505.

Shearer, P. M. (2019). *Introduction to Seismology*, Cambridge University Press, Cambridge, United Kingdom.

Wen, L., J. Badal, and J. Hu (2019). Anisotropic H-κ stacking and (revisited) crustal structure in the southeastern margin of Tibet, *J. Asian Earth Sci.* **169,** 93–104.

Withjack, M. O., R. W. Schlische, and P. E. Olsen (2012). Development of the passive margin of Eastern North America: Mesozoic rifting, igneous activity, and breakup, in *Regional Geology and Tectonics: Phanerozoic Rift Systems and Sedimentary Basins*, Roberts, D. G., and A. W. Bally (Editors), Elsevier, Amsterdam, The Netherlands, 301–335.

Xie, J., M. H. Ritzwoller, S. Brownlee, and B. Hacker (2015). Inferring the oriented elastic tensor from surface wave observations: Preliminary application across the western United States, *Geophys. J. Int.* **201,** no. 2, 996–1021.

Xie, J., M. H. Ritzwoller, W. Shen, Y. Yang, Y. Zheng, and L. Zhou (2013). Crustal radial anisotropy across eastern Tibet and the western Yangtze Craton, *J. Geophys. Res.* **118,** no. 8, 4226–4252, doi: 10.1002/jgrb.50296.

Zhu, L., and H. Kanamori (2000). Moho depth variation in southern California from teleseismic receiver functions, *J. Geophys. Res.* **105,** no. B2, 2969–2980.